Proceedings of ASME Turbo Expo 2025
Turbomachinery Technical Conference and Exposition
GT2025
June 16-20, 2025, Memphis, Tennessee

GT2025-153875

DESIGN AND TESTING OF A TRL-3 OPEN ROTOR STAGE FOR AEROACOUSTICS AND AEROMECHANICS RESEARCH

Kelvin M. Figueroa-Ibrahim[1,*]
Jacob S. Gold[2], Daniel L. Sutliff[2], Clifford A. Brown[1],
Ryne K. Wang[3], Ian B. Martin[3], Mark H. Ross[3], Scott C. Morris[3]

[1]Oak Ridge Associated Universities,TN
[2]NASA Glenn Research Center, Cleveland, OH
[3]Notre Dame Turbomachinery Laboratory, South Bend, IN

ABSTRACT

The NASA Advanced Noise Control Fan Facility (ANCF) was used with a new open-rotor test article. The goal was to understand the test article design space such that the salient aeroacoustic and aeromechanical characteristics of a modern open-rotor engine design were represented. The facility was operated in an outdoor environment where the ambient conditions were uncontrollable. A design advance ratio of $J = 0.325$ was selected based on a statistical analysis of historical ambient data at the outdoor test site. A multi-fidelity design loop allowed a rotor blade design that mimicked the blade loading and tip vortex trajectory of a reference design representing take-off conditions associated with an advance ratio of $J = 1.0$. Results from outdoor experiments involving the rotor blades are presented. The experiments consisted of fixed fan speed, rotor blade pitch and variable advance ratio and angle of attack. The configurations and measurements were limited as this entry was intended to evaluate the proof-of-concept and initial operating capability. Wind, far-field radiated noise, and rotor blade strain measurements are described.

Keywords: Aeroacoustics, Aerodynamics, Open rotor noise, Computational Fluid Dynamics (CFD), Fan noise, Flow-induced vibration and noise

1. MOTIVATION

Open-rotor engine architectures are becoming more relevant for the future of sustainable aviation. An engine with an open-rotor fan architecture provides propulsive efficiency benefits along with reduced weight and drag by excluding the fan nacelle compared to a traditional turbo-fan engine architecture. An increase in the propulsive efficiency of the engine represents a reduction in its fuel consumption. However, open-rotor engine architectures produce noise levels greater than turbofan engine architectures and lack the space to install acoustic liners. In addition, the blades of an open-rotor fan have an increased risk of self-excited or forced vibration than the fan blades of a turbofan engine. The aeroacoustics and aeromechanics issues of open-rotor engines represent significant challenges that will require both fundamental and applied research and development efforts over the next 20 years.

NASA's Efficient Quiet Integrated Propulsors (EQuIP) Technical Challenge [1] aims to accelerate the development of advanced propulsion systems for subsonic aviation by addressing propulsion acoustics and improving technology readiness level (TRL). The challenge emphasizes enabling the adoption of open-rotor systems across the full range of TRLs while overcoming barriers posed by current design limitations. Low TRL facilities are critical in this endeavor by providing insight that enables high-risk concepts to be successful at higher TRLs, providing validation for models and simulations, and investigating risk mitigation technologies. Currently, there is no low TRL facility for open-rotor propulsion research.

The Advanced Noise Control Fan (ANCF) [2, 3] is a NASA-owned, low TRL facility (TRL $\sim$ 3) operated by the Notre Dame Turbomachinery Laboratory (NDTL) at the University of Notre Dame. The ANCF is a ducted fan testbed for studying fan-generated aero-acoustics, duct propagation, and radiation to the far-field[1]. The ANCF was developed and used by the Aeroacoustic Propulsion Laboratory (AAPL) facilities at NASA's Glenn Research Center for 20 years until it was transferred to the University of Notre Dame in 2017 [4]. The ANCF facility was re-purposed to accommodate open-rotor test articles under the EQuIP Technical Challenge [5]. The re-purposing efforts included the design of a new open-rotor fan. The open-rotor ANCF (OR-ANCF) is open-source and publicly available intended to be

*Corresponding author: kelvin.m.figueroa-ibrahim@nasa.gov
NASA Post-doctoral Researcher

[1]The ANCF is a low speed fan, and as such Reynold's number and pressure rise are not relevant in the aforementioned areas of study it is utilized for. Trip strips on the fan blades are used to control transition.

Documentation for `asmeconf.cls`: Version 1.38, March 9, 2025.

utilized for proof-of-concept designs, instrumentation development, and/or code verification. The test article described in this paper includes a rotor-only configuration – stator vane installation and evaluation will be presented in the future. The design philosophy of the OR-ANCF test article prioritized the reproduction of the flow physics and acoustic field generated by open-rotor engine architectures instead of geometrically scaling down an existing modern open-rotor engine design.

The ANCF facility operates in an outdoor environment at the University of Notre Dame [4]. Testing in an outdoor environment poses a complication compared to testing in an enclosed environment. The complication is the lack of control over the ambient conditions, such as the wind speed and direction. These conditions represent independent variables of interest during outdoor testing of an open-rotor facility. The wind speed determines the advance ratio of an open-rotor test article for a fixed fan speed. The advance ratio J is defined as

$$J = \frac{V}{nD}, \tag{1}$$

where V is the free-stream speed in meters per second, n is the fan speed in revolutions per second, and D is the fan diameter in meters. The advance ratio characterizes the flow field around an open-rotor fan. Lack of control over the wind speed translates to a lack of control over the advance ratio, and thus the flow field, for a fixed fan speed. This complication will not be unique to the OR-ANCF and will persist at higher TRL facilities conducting outdoor tests. Therefore, there is an opportunity to implement the methods used to address the issue for OR-ANCF outdoor tests on subsequent full-scale static engine testing.

The goal of the work presented in this paper was to evaluate the re-configuration of the OR-ANCF. The objectives of the work were to demonstrate the initial operating conditions of the test article and to show that an open-rotor facility can be successfully operated outdoors for advance ratios $J > 0$ despite a lack of control over wind conditions. The issues posed by the lack of control over the ambient conditions were addressed with a statistical analysis of historical ambient data for the ANCF test site. The result of the analysis allowed the selection of a design advance ratio that represented a trade-off between desired flow field characteristics and their likelihood which are discussed in the Ambient Conditions section. A proof-of-concept rotor was designed by using a multi-fidelity design loop and is described in the Test Article Design section. Outdoor tests were conducted with the proof-of-concept test article to show relevant aeroacoustic and aeromechanic responses. The results are discussed in the Results section and include wind, radiated noise, and blade vibration measurements.

2. FACILITY DESCRIPTION

Figure 1 shows the ANCF at the University of Notre Dame in the outdoor testing facilities. The ANCF is powered by a 149 $kW(200\ hp)$ electric motor and its nominal fan speed is 1800 RPM. It is composed of highly configurable outer spools that comprise the duct and a center-body that is cantilevered from a U-shaped support structure. The diameter of the duct is 1.22 m and the length can be varied by installing or removing spool

FIGURE 1: THE ADVANCE NOISE CONTROL FAN FACILITY AT THE UNIVERSITY OF NOTRE DAME TEST SITE.

sections of lengths between 30 $cm(12\ in.)$ and 33 $cm(13\ in.)$. An inflow control device (ICD) is shown integrated into the inlet lip for flow conditioning. Further details about the ANCF can be found in Sutliff [2].

Figure 2 shows a CAD model of the open-rotor test article installed on the ANCF facility. The installation of a new open-rotor test article on the ANCF was achieved with minimal changes to the existing drive system and infrastructure. The new test article consisted of a rotor assembly followed by a stator assembly. The rotor assembly had a diameter of 1.0764 $m(3.53\ ft.)$ and comprised 10 new rotor blades and a new rotor hub. The rotor blades were comprised of NACA 4415 airfoils from the hub to 25% span, NACA 4412 airfoils from 25% to 50% span, NACA 4410 airfoils from 50% to 75% span, and NACA 4408 airfoils from 75% to the tip. The rotor blades and hub were machined from aluminum $6061 - T6$ and had mean stress safety factors of 3.3 and 2.0, respectively. Safety factors were defined for an operating fan speed of 1800 : RPM. The safety factors for the rotor blades and the rotor hub increase to 7.5 and 4.5 for an operating fan speed of 1200 : RPM. The stator assembly had a diameter of 1.046 $m(3.43\ ft.)$ and comprised 7 new stator vanes installed on the existing stator hub of the ANCF. The stator vanes were comprised of NACA 4415 airfoils from the hub to 25% span, NACA 4412 airfoils from 25% to 50% span, NACA 4410 airfoils from 50% to 75% span, and NACA 8412 airfoils from 75% to the tip.

A containment system was designed for the OR-ANCF and is also shown in Fig. 2. The containment system comprised an aluminum mounting plate, aluminum clamping plates, and an aluminum frame that supported layers of dry Kevlar cloth. It was designed to capture a rotor blade in the unlikely event of a blade-out. The Kevlar properties were based on experiments and computations by Xuan et al. [6]. The Kevlar cloth had a layer thickness of 0.33 $mm(0.013\ in)$, a width of 1.27 $m(50\ in)$ a yarn denier of 1420 $g/9km$, and a plain weave pattern. The Kevlar cloth was stretched to a tension of 25 $N(5.6\ lbs.)$. The Kevlar width was chosen to cover a $\pm 15°$ arc measured from the rotor plane. The $\pm 15°$ arc represents the potential spread of a released blade from the OR-ANCF. The $\pm 15°$ arc is recommended by the

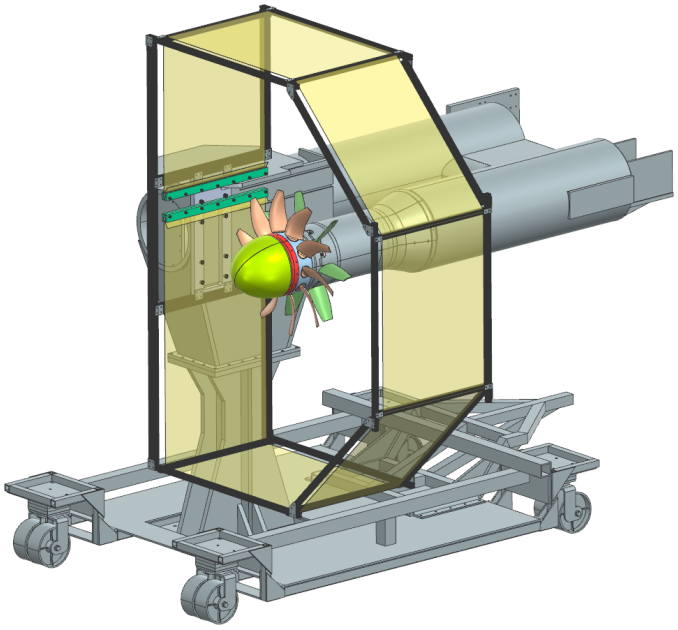

FIGURE 2: THE OPEN-ROTOR ANCF TEST ARTICLE AND CONTAINMENT SYSTEM.

U.S. Department of Transportation [7] and has been used for similar open-rotor test articles designs in the past [8]. Six layers of Kevlar were stacked together to achieve a total thickness of $1.98\,mm(0.078\,in)$. The total thickness of the Kevlar was chosen to have a minimum safety factor of 2 at stopping a released blade. The safety factor was defined based on the kinetic energy of a released blade during an operational fan speed of $1800\,RPM$. The selection of the total thickness of the Kevlar was based on similar work on composite containment systems for the containment of jet engine fan blades [9–11].

The OR-ANCF was equipped with systems to measure the ambient wind conditions, the radiated noise, and the rotor blade vibrations. A Sonic Anemometry System (SAS) was used to measure and monitor the ambient wind conditions. The SAS comprised two 3D ultrasonic anemometers by Thies Clima mounted on tripods and connected to a single data logger DLU E unit by Thies Clima. The anemometers provide three-components of wind speed and direction. They have a speed range of 85 m/s with an accuracy of $\pm 0.1\ m/s + 1\%$ of measured value for wind speed below 35 m/s. They have a wind direction range of 360° with an accuracy of ±1° for wind speed below 35 m/s. The data logger can record data at a rate of up to 1 Hz. One anemometers was placed upstream of the ANCF at a distance R of $6.1\,m(20\,ft.)$ from the rotor inlet plane and aligned with the shaft centerline. The other anemometer was placed $1.5\,m(5\ ft)$ to the right of the first anemometer.

A Health Monitoring System (HMS) was designed to measure and monitor in real-time of the mean and fluctuating rotor blade strains during operation. The HMS comprised a battery-powered blade strain telemetry system, provided by Advanced Telemetrics Inc., connected to strain gauges on the rotor blades. The telemetry system had 5 Model 3140B-2, two-channel strain gauge transmitter, and a Model 3MRB-12000 rechargeable battery pack housed on a Model 2110i-5SP single-piece telemetry collar. The telemetry collar was installed on the rotor hub and allowed transmission of the telemetry RF signals through the fiberglass nose cone. The RF signals were received by a Model 3125B-10, 10-channel telemetry receiver connected to a RX-3X antenna via a Model 1028D-20 antenna-to-receiver cable. The strain gauges were Omega SGT-3N/350-TY43 $350\,\Omega$ linear strain gauges with a gain factor of 2.09. The strain gauges were connected to the transmitter via lead wire. Each rotor blade had one strain gauge installed for a total of 10 strain gauges used. The strain gauges were placed on the pressure side of the blades. The strain gauges were placed on one of two distinct locations over the rotor blades. Location 1 was at $11.16\,mm(0.44\,in.)$ from the leading edge in the chord direction and $0.34\,mm(0.013\,in.)$ from the root along the span. Location 2 was at $3.98\,mm(0.16\,in.)$ from the leading edge along the chord direction and $0.9\,mm(0.035\,in.)$ from the root along the span direction. The locations were selected based on vibrational mode visibility calculations. The visibility was calculated as the ratio of the equivalent Von-Mises strain to the maximum Von-Mises strain of a given vibrational mode at multiple, discrete locations over the blade surface. The two locations with higher visibility across multiple modes and closer to the blade root were chosen. The visibility calculations for the two locations are shown in Table 1.

TABLE 1: VISIBILITY MATRIX FOR THE PLACEMENT OF STRAIN GAUGES ON THE ROTOR BLADES.

Location	Mode 1	Mode 2	Mode 3	Mode 4
1	90%	90%	34%	61%
2	65%	24%	82%	93%

The noise radiated by the test article was measured by two far-field microphones. The microphones used were PCB Piezotronics 130D20 $6.35\,mm(1/4\,in.)$ pre-polarised, condenser microphone. They have a free-field frequency response characteristic with ± 1 dB from 100 to 4000 Hz and ± 2 to 5 dB from 20 to $15,000\,Hz$. The microphones were mounted on ground plates as shown in Fig. 3. The ground plates perfectly reflect the incoming sound wave from the test article. The distance between the plate and the microphone induce constructive interference of the incoming and reflected sound waves at the location of the microphone. The microphones were placed upstream of the ANCF at a distance R of $5.3\,m(17.5\ ft.)$ from the rotor inlet plane. The microphones were placed at polar locations of $\theta = 0°$ and $\theta = 11.2°$ measured from the projection of the shaft centerline on the ground.

The radiated noise was also measured by a phased array of microphones deployed during the first experimental campaign of the OR-ANCF. The phased array was the ACAM 120 Acoustic Camera from OptiNAV Inc. and Signal Interface Group (SIG). The array comprised 40 PCB microphones embedded on a $50cm(19.6in)$ square panel and a digital camera located at its center. The beam-forming results were superimposed on the optical image from the camera in real time and allowed visualization of the acoustic field. The 40 microphones were simultaneously sampled with 24-bit resolution via an onboard Field Programmable Gate Array (FPGA) at $50kHz$ and have a dynamic range of $125dB$.

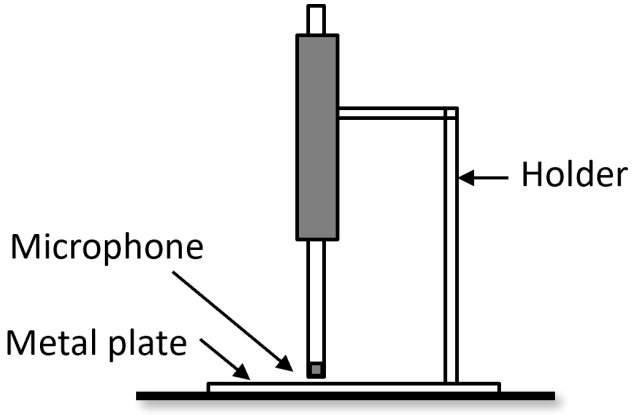

FIGURE 3: GROUND MICROPHONE ASSEMBLY COMPRISING A MICROPHONE, HOLDER, AND METAL PLATE.

The geometry and microphone sensitivity of the array provided a working bandwidth from 60 Hz to 15 kHz. Frequencies up to 23 kHz were measured with reduced amplitude accuracy. Processing was performed using OptiNAV's Function Beamforming algorithm.

3. EXPERIMENTAL METHOD

The OR-ANCF was built and operated at the traditional ANCF test site. The fan was oriented to point towards the Southeast direction, at 150° relative to the North direction. The fan orientation coincided with the direction of the incoming wind. The microphone and strain gauge data were sampled at 50 kHz using an HBM GEN3i Genesis data recorder system. The SAS datalogger collected wind measurements for the full duration of the test at a rate of 1 Hz. The sonic anemometers were aligned with the North direction so that their readings are defined at 0° in that direction. The tests consisted of fixing the fan speed and acquiring data for periods of 5 min.

The microphone and strain gauge data were averaged over periods of a second that featured a steady advance ratio. The Auto-Spectral Density (ASD) was calculated for multiple periods via a welch calculation using the open-source Python library SciPy. The ASD calculation featured segment lengths of 16, 384 data points, a hanning window with 50% overlap, and a number of Fourier Transform coefficients of 16, 384. The Sound Pressure Level (SPL) for the measured radiated noise was calculated from the ASD as

$$SPL = 10 * log_{10}\left(\frac{ASD * df}{P_{ref}^2}\right), \tag{2}$$

where the SPL is in dB, the ASD is in $\frac{Pa^2}{Hz}$, df is the frequency resolution of the spectrum, and $P_{ref} = 2e^{-5}\ Pa$.

The wind direction measurements collected by the SAS were used to define a wind alignment to the OR-ANCF facility. The wind alignment was defined as

$$\theta_{align.} = \theta_{wind} - \theta_{ANCF}, \tag{3}$$

where θ_{wind} is the measured wind speed by the anemometer in degrees and θ_{ANCF} is the direction to which the OR-ANCF was aligned in degrees. Values of $\theta_{align.}$ of zero show perfect alignment of the wind with the OR-ANCF test article. Values other than zero show a misalignment to the OR-ANCF. A wind alignment threshold of ±5° was defined. The wind alignment threshold was used to segregate measurements and identify data periods corresponding to wind alignment to the direction of the OR-ANCF test article.

4. AMBIENT CONDITIONS

The OR-ANCF tests meant to study the flow and acoustic fields around an open-rotor test article at operational conditions of interest. One operational condition of interest for commercial open-rotor engines is during aircraft take-off. The flow field around open-rotor engines during take-off is associated with an advance ratio of 1. The lack of control over the ambient conditions at the ANCF test site makes it difficult to match the advance ratio of interest in any given instant. A statistical analysis was conducted on historical wind data for the ANCF test site to reveal the most likely advance ratio on any given day of outdoor testing. Learning the most likely advance ratio allowed the selection of a design advance ratio based on a design fan speed.

There were three sonic anemometers installed on a meteorological tower near the ANCF test site. The sonic anemometers were at heights of $6m(19.7\,ft)$, $10m(32.8\,ft)$, and $16m(52.5\,ft)$ from the ground. The anemometers recorded wind speed and direction at a rate of $1/60$ Hz from 2019 to 2023. The statistical analysis was conducted using the data corresponding to the sonic anemometer closer to the ground. The data were filtered to include values contained within the times of day associated with traditional ANCF testing periods. The traditional ANCF test periods comprised the months of April to October and the hours of $10:00\ am$ to $5:00\ pm$.

Figure 4 shows a histogram of the filtered sonic anemometer data. The abscissa shows wind speed bins in mph. The wind speed bins have a width of 1 mph. The ordinate indicates the number of values on a given wind speed bin. The distribution has a mean value of 4 mph and a maximum value of 34 mph. For reference, 0 mph is associated with calm conditions, 4 mph is associated with leaves rustling and small twigs moving, and 34 mph is associated with large tree branches in continuous motion. The distribution is skewed towards the low wind speed values. The distribution resembles a Weibull distribution and is consistent with typical ambient wind measurement distributions [12]. These data suggest that wind speed values significantly greater than zero can be obtained in an outdoor environment despite the lack of control.

The historical wind data were used in conjunction with the fan speed capabilities of the ANCF to determine the most likely advance ratio on any given day of testing and are shown in Fig. 5. The abscissa shows the advance ratio J and the ordinate shows the maximum fan speed in RPM. The contour lines show the probability of getting an advance ratio at a specific fan speed on any given day in percentages. The contour lines indicate that an advance ratio of 1 can be achieved at the test site only at fan speeds below 500 RPM. However, the noise levels generated by an open rotor fan are a function of its rotational speed. The noise levels produced by fan speeds less than 500 RPM do not

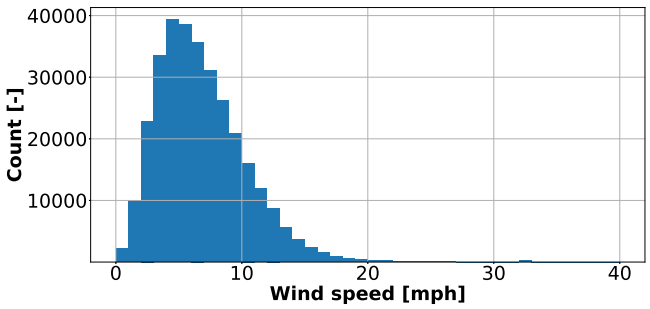

FIGURE 4: HISTOGRAM OF WIND SPEED HISTORICAL DATA FOR THE ANCF TEST SITE.

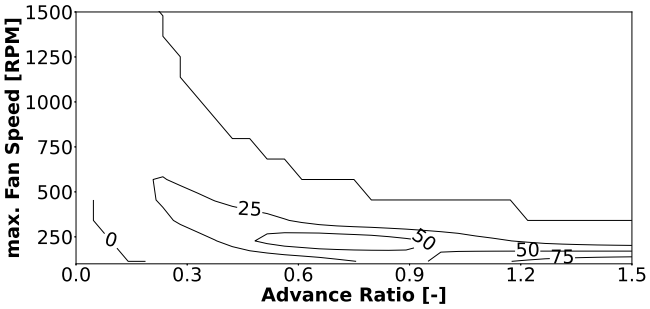

FIGURE 5: CONTOUR PLOT SHOWING THE PROBABILITY OF FINDING AN ADVANCE RATIO FOR A GIVEN FAN SPEED ON A GIVEN DAY OF ANCF TESTING.

align with the acoustics produced by commercial aircraft at take-off conditions. The radiated noise produced by the ANCF rises above the background noise at fan speeds above 800 RPM. The contour lines in Fig. 5 indicate that fan speeds of up to 1000 RPM can be found at lower advance ratios. This suggests that the rig can produce relevant noise levels by limiting the advance ratio that can be achieved. An advance ratio of 0.325 was chosen as the trade-off between relevant noise levels and the desired characteristics of the incoming flow field. The statistical analysis showed that relevant acoustic can be produced at relevant advance ratio values at the test site despite the lack of control over the ambient conditions.

5. TEST ARTICLE DESIGN

The rotor blades for the OR-ANCF test article were designed using an iterative procedure shown in Fig. 6. The design procedure followed a multi-fidelity design and analysis loop inspired by Siddappaji and Turner [13]. The procedure began with a low-fidelity Actuator Disk Theory calculation. The Actuator Disk Theory modeled the rotor as an infinitesimally thin disk that exerted a force upon the fluid. The Actuator Disk Theory allowed the calculation of the thrust and power exerted on the ingested fluid. The loop progressed into a 2D Blade Element Momentum Theory (BEMT) calculation. The BEMT calculation allowed the actuator disk to be discretized into several blades. The blades were divided into spanwise slices and accounted for spanwise airfoil characteristics and local flow properties and gave a better

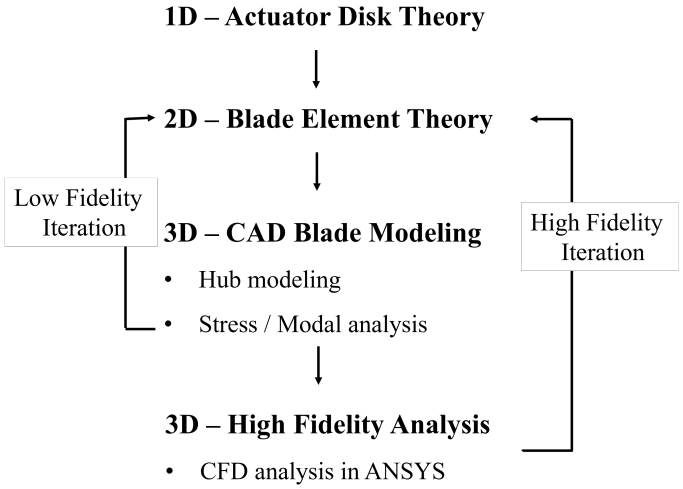

FIGURE 6: MULTI-FIDELITY DESIGN LOOP USED TO DESIGN THE OR-ANCF ROTOR BLADES.

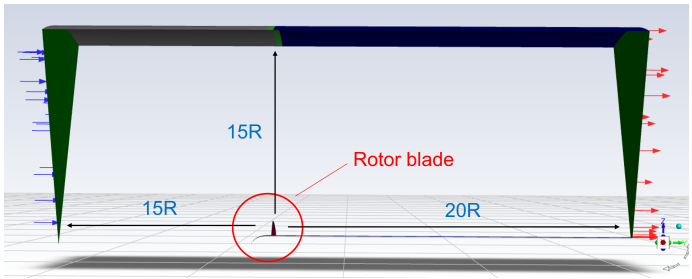

FIGURE 7: DOMAIN USED FOR THE CFD SIMULATIONS IN THE DESIGN LOOP.

prediction of local aerodynamic forces and torque. The BEMT results allowed the creation of a 3D CAD model of the blade.

The 3D CAD model of the blade was used for Finite Element Method (FEM) stress and modal analyses in the following step. The FEM calculation was conducted in Ansys and revealed the natural frequencies and vibrational modes of the rotor blades along with the locations of peak mean stresses. The final step was a high-fidelity, 3D CFD simulation that captured the flow-structure interactions in greater detail. The CFD analysis consisted of a Reynolds-Averaged Navier Stokes (RANS) simulation in Ansys Fluent. A single-sector 3D CFD domain consisting of a 36° circumferential segment was modeled and is shown in Fig. 7. The domain featured 1.25 million grid cells. A grid-dependency study was conducted to determine the size of the CFD domain that minimized boundary effects on the flow regions of interest. Periodic boundary conditions were applied on both sides of the sector. The remaining boundary conditions are composed of an inlet 15 chords upstream, an upper boundary 15 spans away, and an outlet 20 chords downstream of the blade. The CFD simulation results were fed back into the lower-fidelity design loop for iterative refinements on blade design until established design criteria were met.

There were aerodynamic, aeroacoustic, and aeromechanical design criteria defined for the OR-ANCF rotor blades. The aero-

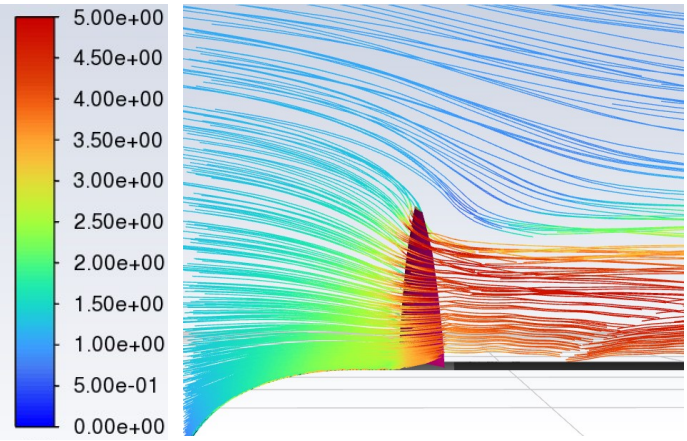

FIGURE 8: PATHLINES AROUND THE OR-ANCF ROTOR BLADES FOR THE DESIGN ADVANCE RATIO J = 0.325.

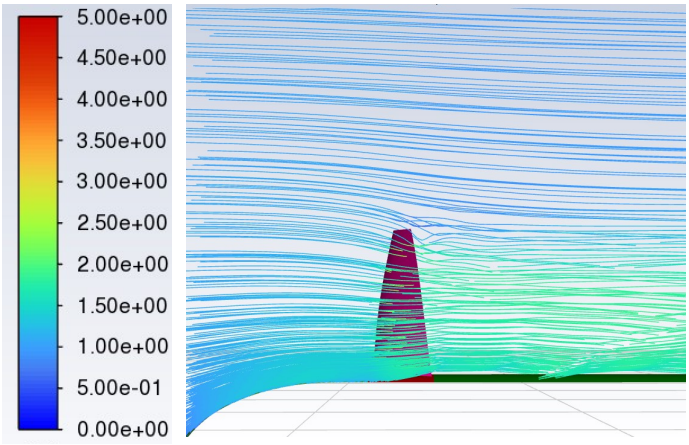

FIGURE 9: PATHLINES AROUND THE OR-ANCF ROTOR BLADES FOR THE REFERENCE ADVANCE RATIO J = 1.0.

dynamic criterion was to design a rotor blade to operate in a flow field characterized by an advance ratio of $J = 0.325$. This criterion ensured the rotor blade could operate at the ANCF test site under the expected conditions. A simulation corresponding to an advance ratio of $J = 1.0$ was conducted as a reference case. The blade design simulations were compared to the reference case to observe the differences in the flow field and evaluate the aeroacoustic design criterion. The reference simulation was for a fan speed of 1800 RPM and a free-stream speed of 32 m/s. The reference case represented nominal take-off conditions. The blade design simulations were conducted for the advance ratio of $J = 0.325$ corresponding to a fan speed of 1800 RPM and a free-stream speed of 10 m/s. The chord-based Reynolds number for the design simulation was 6.5 x 10^5.

Figure 8 and Fig. 9 show CFD images of the flow field for both reference and final blade design simulations. Figure 8 corresponds to the final blade design simulation and Fig. 9 corresponds to the reference case. The figure shows pathlines around the rotor blades. The pathlines were seeded at a plane coinciding with the tip of the nose cone of the test article. The pathlines are colored based on the normalized flow speed. The flow speed was normalized by the free-stream wind speed of 10 m/s. Blue is associated with a value of 0 and red is associated with a value of 5. Figure 9 shows relatively straight pathlines traveling around the rotor in the downstream direction. The pathlines in 9 show slight curvature around the rotor blade tips. Figure 8 shows more prominent pathline curvature as the flow is ingested by the rotor. The pathline curvature observed in Fig. 8 is associated with a contraction of the streamtube ingested by the rotor and is a product of the lower advance ratio.

The aerodynamic loading on a blade designed for an advance ratio of $J = 1$ would be altered significantly if it were operated in an advance ratio of $J = 0.325$. The geometric features of the blade design for an advance ratio of $J = 0.325$ were meticulously altered across several iterations in the design loop to alleviate the differences in aerodynamic loading. The blade design featured a different angle of attack distribution as a function of span and tip geometry. The blade design with these geometric features that operated in an advance ratio of $J = 0.325$ produced a thrust of 84 N and a lift of 96.1 N. The thrust and lift for the blade that operated in an advance ratio of $J = 1$ were 80.4 N and 103.8 N, respectively. The thrust and lift difference between the two cases was 4.4% and 7.7%, respectively. These metrics show that the two blade designs had similar aerodynamic loading despite the notable differences in their respective flow fields.

The aeroacoustic design criterion was for the test article to generate an acoustic signature at an advance ratio of $J = 0.325$ similar to commercial aircraft take-off conditions. The criterion was evaluated by comparing the flow features at the blade surface that are associated with the acoustic pressure radiated to the far-field between the design and reference CFD cases. The flow features compared were the tip vortex impingement on the rotor blade surface and the mean surface pressure distribution on the rotor blade surface. Figure 10 shows the design simulation on the left and the reference simulation results on the right. Figure 10 shows contours of the pressure coefficient C_p at the blade surface. The pressure coefficient was calculated as

$$C_p = \frac{P}{1/2\left(U_{tip}^2 + U_\infty^2\right)}, \tag{4}$$

where P is the mean static pressure at the blade surface in Pa, ρ is the fluid density in kg/m^3, U_{tip} is the blade tip speed in m/s, and U_∞ is the free-stream speed in m/s. The colorbar shows a range from -2.042 to 0.1257. The blue colors are associated with the low extreme of the pressure coefficient values while red is associated with the high extreme of the pressure coefficient values. There are also white lines showing iso-contours of pressure coefficient. The reference simulation shows most of the blade surface is dominated by red colors. This shows most of the blade features a higher pressure coefficient. The leading edge region in both cases features yellow and blue colors. This region shows lower pressure coefficient along the leading edge in both cases. The region of lower pressure coefficient on the design case is observed roughly from 30% span to the tip. The region of lower pressure coefficient on the reference case is observed roughly from 50% span to the tip. The white iso-contour lines show agreement between the set of blades. These observations

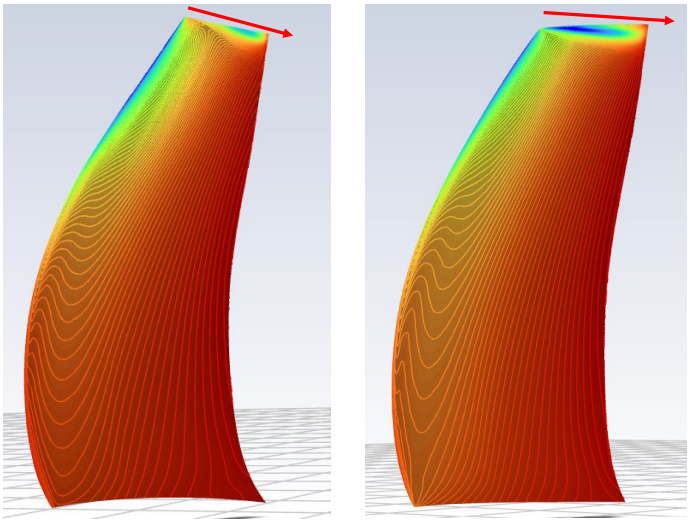

FIGURE 10: CONTOURS OF SURFACE PRESSURE ON THE PRESSURE SIDE OF THE ROTOR BLADE. A) DESIGN CASE OF ADVANCE RATIO J = 0.325. B) REFERENCE CASE OF ADVANCE RATIO J = 1.0.

show a similar mean surface pressure field in both CFD cases. The hypothesis is that the matching mean blade surface pressure distribution will be associated with similar radiated acoustic pressure levels in both cases.

There is also a region of blue color along the tip of both the reference and design blade. This region is associated with the tip vortex generated at the tip of the blade. Red arrows are shown superimposed on the CFD image to show the tip vortex trajectory. The tip of the design blade is different from the reference blade. The reference blade shows a flat surface at the top, whereas the design blade features a 20° angular cut highlighted in the figure. The tip cut angle follows the streamtube contraction such that it would create a surface of revolution coincident with the stream tube. The tip cut provides control over the impingement of the tip vortex on the blade. Too much interaction, which would be caused by a shallow tip cut, would cause excessive noise generation whereas too little interaction, caused by a sharp tip cut, would inhibit noise generation. Inhibiting noise generation would not meet the aeroacoustic design criteria of generating noise similar to the reference blade.

The aeromechanic design criterion was to ensure the natural frequencies of the rotor blades were greater than the known excitation frequencies during ANCF nominal operation. The results from the FEM modal analysis were used to evaluate the aeromechanical design criteria and are shown in Table 2. The columns in Table 2 show the frequencies associated with the different modes of vibration. The rows in Table 2 correspond to the harmonics of each of the vibrational modes. The cells in the matrix show the frequencies for a particular harmonic of the vibrational mode in Hz. These values were compared to the known excitation frequencies associated with the operation of the ANCF facility. The ANCF nominal operation corresponds to a fan speed of 1800 RPM, or a frequency of 30 Hz. There will be 7 stator vanes installed downstream of the rotor when the full test article is installed. In that configuration, the rotor blades will

TABLE 2: VIBRATIONAL MODE FREQUENCIES AND THEIR HARMONICS.

Harmonic index	Mode 1	Mode 2	Mode 3
0	235 Hz	643 Hz	667 Hz
1	228 Hz	484 Hz	658 Hz
2	223 Hz	481 Hz	657 Hz
3	235 Hz	649 Hz	736 Hz

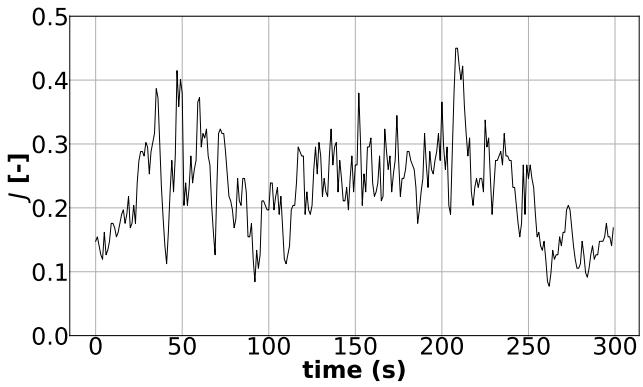

FIGURE 11: TIME-SERIES OF ADVANCE RATIO DURING OR-ANCF OUTDOOR TESTING FOR A FIXED FAN SPEED.

perceive an excitation at a rate of the fan speed times the number of stator vanes. The excitation frequency perceived by the rotor blades is 210 Hz. The values listed in Table 2 are all greater than these known excitation frequencies. That means the excitation of the stator vanes on the rotor blades will not lock on to any natural frequencies within the fan speed range of the ANCF facility. Thus, the blade designed for the OR-ANCF test article met the aeromechanical design criterion.

6. RESULTS

6.1 Ambient wind measurements

Figure 11 and Fig. 12 show time series of ambient wind conditions collected during the OR-ANCF outdoor tests. These data were collected at a fan speed of 800 RPM. The abscissa shows time in $sec.$. The ordinate in Fig. 11 shows the advance ratio J. For a fixed fan speed, variations in advance ratio are associated with variations in the incoming wind speed only. Each data point represents an average over a second of data collection. Figure 11 shows the advance ratio ranged from 0.06 to 0.44 over a period of 300 $sec.$. The advance ratio values obtained were greater than the design advance ratio of 0.325 during certain periods. These periods had durations from 2 $sec.$ up to 5 $sec.$.

The ordinate in Fig. 12 shows wind alignment $\theta_{align.}$ in degrees. The range of the ordinate in Fig. 12 is from $-15°$ to 15°, although there were values recorded beyond this range. There are two solid, horizontal, red lines shown in Fig. 12. These lines highlight the wind alignment threshold of ±5°. The time series shows short periods within the alignment band. The periods within the alignment band lasted from 1 $sec.$ up to 5 $sec.$. These results show that wind properties of interest, such as steady ad-

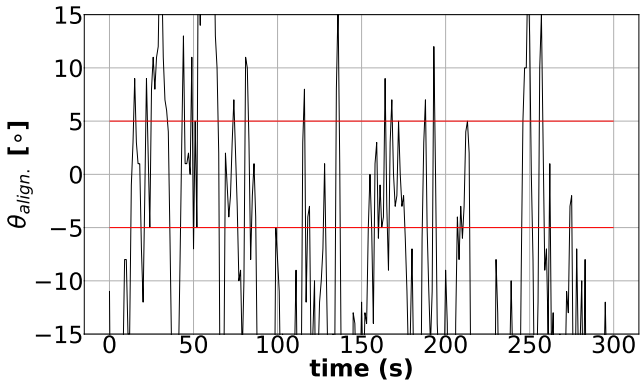

FIGURE 12: TIME-SERIES OF WIND ALIGNMENT DURING OR-ANCF OUTDOOR TESTING FOR A FIXED FAN SPEED.

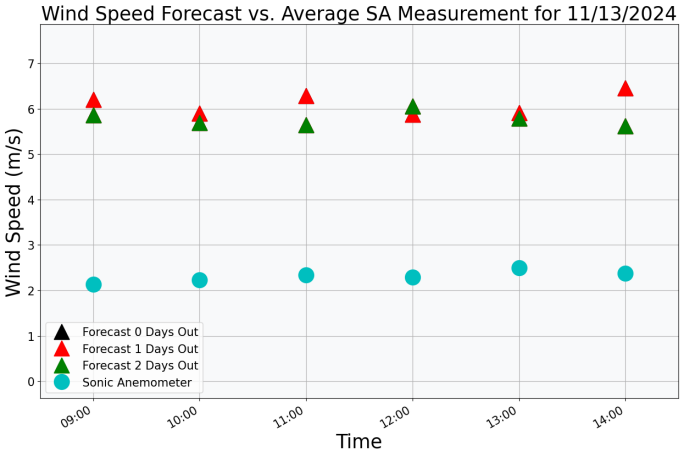

FIGURE 13: COMPARISON OF WIND SPEED FORECAST FOR THE SOUTH BEND AREA AND WIND MEASUREMENTS AT THE OR-ANCF TEST SITE.

vance ratios at wind alignment with the ANCF, can be obtained on a given day of outdoor testing despite a lack of control over them. Allowing long periods of data acquisition increases the likelihood of encountering these periods.

Weather forecasts were consulted during the days leading up to the OR-ANCF outdoor tests to inform the orientation of the rig and the expected wind speeds. Weather forecasts were recorded from the OR-ANCF test days from the OpenWeather website. The recorded information included the wind speed and direction for the South Bend region. The information was recorded up to four days before the outdoor tests. The recorded forecasts were compared to the wind measurements by the sonic anemometers during the outdoor tests and are shown in Fig. 13 and Fig. 14. Figure 13 shows forecast versus measured wind speed comparison. Figure 14 shows the forecast versus measured wind direction.

The abscissa in Fig 13 and Fig. 14 shows the time in time stamps. The time stamps are shown for every hour. The ordinate in Fig. 13 shows the wind speed in m/s. The ordinate in Fig. 14 shows the wind direction in degrees. The forecast data points represent the expected wind quantity over the hour in the time stamp.

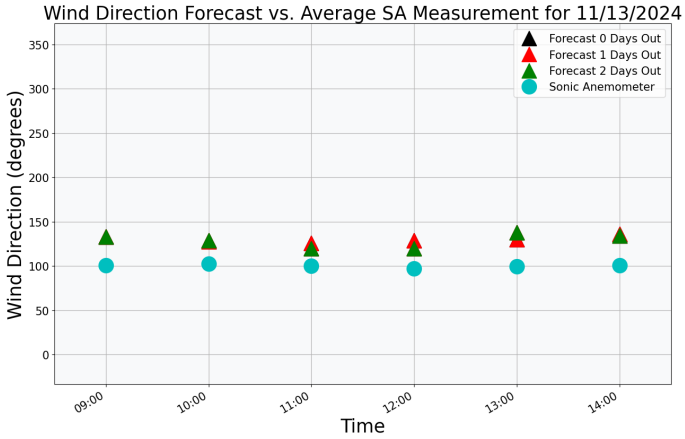

FIGURE 14: COMPARISON OF WIND DIRECTION FORECAST FOR THE SOUTH BEND AREA AND WIND MEASUREMENTS AT THE OR-ANCF TEST SITE.

The sonic anemometer data points represent averages over the hour in the time stamp. The wind direction measurements show values around 100°. The wind direction measurements show little variation throughout the day. The forecast wind direction shows values between 125° and 155°. The forecast wind direction appears to decrease towards the middle of the day and then increase towards the end of the test day.

The wind speed forecast show values between 5 m/s and 6.5 m/s. The wind speed measurements show values between 2 m/s and 3 m/s. There is a discrepancy between the forecast and measured values of up to 4.5 m/s. The discrepancy in the wind speed can be explained by the structures in the vicinity of the ANCF. There is a tree located at the test site. The trunk of the tree was roughly 15.3 $m(50\ ft.)$ upstream of the OR-ANCF during that day of testing. It is possible the wind speeds recorded by the sonic anemometers were consistently lower than the forecasts due to the presence of the tree. The forecast data suggest orienting the ANCF at an angle of $\theta_{ANCF} = 140°$ would give decent alignment throughout the day, whereas the wind measurements suggest the wind was consistently 25° degrees off from the average wind direction forecast for that day.

6.2 Radiated noise

Figure 15 shows the SPL spectrum for microphone 1. The abscissa shows the shaft order. The shaft order is calculated as the frequency divided by the shaft rate in revolutions per second. The shaft rate is calculated dividing the shaft speed in revloutions per minute by 60. The ordinate shows the SPL in dB. Multiple curves correspond to multiple advance ratios. The advance ratios shown are $J = 0.06$, $J = 0.14$, $J = 0.24$, $J = 0.34$, and $J = 0.44$. The fan speed was 800 RPM which provided a blade-passing frequency of 134 Hz. The blade passing frequency corresponds to a shaft order of 10. The data shown featured $\theta_{align.}$ values within the ±5° alignment threshold.

The curves show peaks around shaft orders of 10, 20, 30, 40, and 50. The peaks have widths of roughly ±10% of the center frequency. The first peak shows an amplitude of 71.5 dB for all advance ratio curves. The second peak shows a maximum

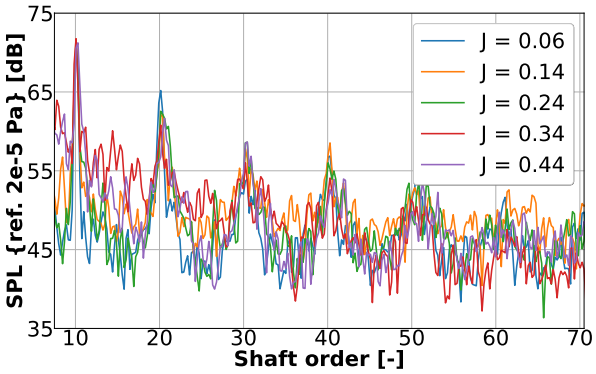

FIGURE 15: RADIATED NOISE SOUND PRESSURE LEVEL SPECTRUM FOR A FAN SPEED OF 800 RPM AND ALIGNMENT $\theta_{align.} = \pm 5°$ BUT VARIABLE ADVANCE RATIO J.

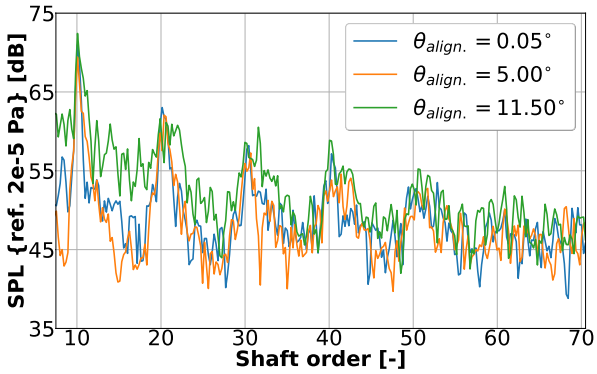

FIGURE 16: RADIATED NOISE SOUND PRESSURE LEVEL SPECTRUM FOR A FAN SPEED OF 800 RPM AND ADVANCE RATIO $J = 0.32$ BUT VARIABLE WIND ALIGNMENT $\theta_{align.}$.

amplitude of 65 dB for an advance ratio of $J = 0.06$ and a minimum amplitude of 58.5 dB for an advance ratio of $J = 0.34$. The third peak shows a maximum amplitude of 57 dB for an advance ratio of $J = 0.44$ and a minimum amplitude of 54 dB for an advance ratio of $J = 0.06$. The fourth peak shows a maximum amplitude of 57 dB for an advance ratio of $J = 0.06$ and a minimum amplitude of 52 dB for an advance ratio of $J = 0.44$. The first peak shows the same amplitude across all advance ratio values. The higher harmonics show different variation as a function of the advance ratio.

The peaks stand above the broadband content of the signal for up to 25 dB at an advance ratio of $J = 0.04$. The peaks show lower amplitudes than the broadband content at some frequencies at an advance ratio of $J = 0.44$. The peaks observed in Fig. 15 are attributed to the blade-passing frequency harmonics, and the amplitude of the peaks corresponds to the tones of the OR-ANCF test article. The width of the peaks is associated with the haystacking of broadband noise. Haystacking occurs when a turbulent structure is stretched axially as it is ingested by the rotor. The stretching of the structure can cause multiple blades to pass through the turbulent structure. This results in a quasi-periodic signal in the acoustic far-field that includes bursts of pulses at the blade-passing frequency and a sound spectrum with broadband peaks at near multiples of the blade-passing frequency [14].

The broadband content of the signal appears to be greater for higher advance ratios. The broadband content between the first three harmonic peaks is dominated by an advance ratio of $J = 0.34$. These observations suggest that the broadband noise generated by the OR-ANCF test article increased as the advance ratio increased. The increase in the broadband content with an increasing advance ratio for a fixed fan speed is consistent with the known noise generation mechanisms of a rotating blade. For instance, trailing edge noise is seen to scale approximately with the fifth power of the flow velocity [14].

Figure 16 shows curves of SPL spectrum calculated from the microphone 1 signals in the same format as Fig. 15. The fan speed was 800 RPM which provided a blade-passing frequency of 134 Hz and shaft order 10. The average advance ratio for the data was $J = 0.32$ which coincides with the design point for the test article. Multiple curves correspond to alignments. The alignments shown are $\theta_{align.} = 0.05°$, $\theta_{align.} = 5.00°$, and $\theta_{align.} = 11.50°$. The curves featured the blade-passing harmonics observed in Fig. 15.

The first peak shows a maximum amplitude of 72.4 dB for an alignment of $\theta_{align.} = 11.5°$ and a minimum amplitude of 69.4 dB for an alignment of $\theta_{align.} = 5°$. The second peak shows a maximum amplitude of 63 dB for an alignment of $\theta_{align.} = 0.05°$ and a minimum amplitude of 57.5 dB for an alignment of $\theta_{align.} = 5°$. The third peak shows a maximum amplitude of 58.5 dB for an alignment of $\theta_{align.} = 11.50°$ and a minimum amplitude of 55 dB for an alignment of $\theta_{align.} = 5°$. The fourth peak shows a maximum amplitude of 58.8 dB for an alignment of $\theta_{align.} = 11.50°$ and a minimum amplitude of 53.8 dB for an alignment of $\theta_{align.} = 5°$. The lowest tonal amplitude across harmonics was observed for an alignment of $\theta_{align.} = 5°$. The greatest tonal amplitude alternated between the alignments of $\theta_{align.} = 0.05°$ and $\theta_{align.} = 11.50°$. The harmonic tones also appear to widen as a function of the alignment angle.

The broadband content appears to increase as a function of the alignment angle. The broadband content increase is observed for shaft orders below 40. The increase in broadband content is more prominent between the first and second harmonic peaks. For instance, the broadband content increased from 46.1 dB at an alignment of $\theta_{align.} = 5.00°$ and 50.8 db at an alignment of $\theta_{align.} = 0.05°$ to 60.9 db for an alignment of $\theta_{align.} = 11.50°$. These observations suggest that an increase in the wind alignment angle, which means the wind deviates from the OR-ANCF shaft centerline, causes an increase in the broadband noise generated by the test article. An increase in the alignment translates to a change in the angle of attack of the rotor blades. Higher angles of attack may thicken and intensify the turbulent blade flow, thus increasing the radiated sound, particularly at low frequencies [15]. Measurements from Brooks and Hodgeson [16] showed increases in the low-frequency noise as the angle of attack of a NACA 0012 airfoil was increased to 6°. Broadband noise increase caused by an increase in the angle of attack of the OR-ANCF rotor blades can explain the increase in broadband levels in Fig. 16.

Figure 17 shows curves of SPL spectrum calculated from the

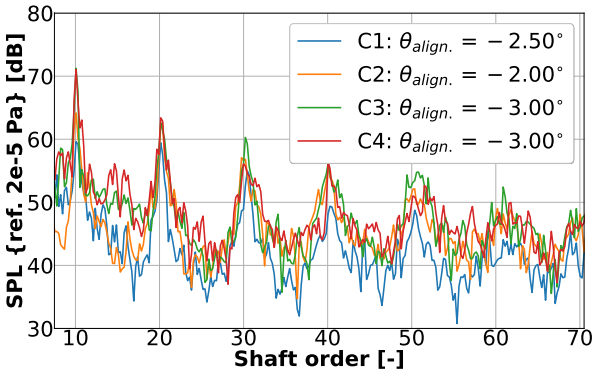

FIGURE 17: RADIATED NOISE SOUND PRESSURE LEVEL SPECTRUM FOR A FAN SPEED OF 800 *RPM*, AN ADVANCE RATIO J = 0.27, AND RELATIVELY STEADY WIND ALIGNMENT.

FIGURE 18: OVERALL SOUND PRESSURE LEVEL FIELD FOR A FAN SPEED OF 800 *RPM*, AN ADVANCE RATIO J = .19, AND WIND ALIGNMENT $\theta_{align.} = -5°$.

microphone 1 signals in the same format as Fig. 15. The fan speed was 800 RPM and provided a blade-passing frequency of 134 Hz and shaft order of 10. The average advance ratio for the data was $J = 0.27$. Multiple curves correspond to different alignments. The alignments shown are $\theta_{align.} = -2.00°$, $\theta_{align.} = -2.50°$, $\theta_{align.} = -3.00°$, and $\theta_{align.} = -3.00°$ and were chosen to have values relatively close to each other. The selection intended to provide data at a fixed advance ratio and wind alignment.

The curves featured the blade-passing harmonics observed in Fig. 15. The first peak shows a maximum amplitude of 71.2 dB on curve 3 and a minimum amplitude of 59.6 dB on curve 1. The second peak shows a maximum amplitude of 63.4 dB on curve 4 and a minimum amplitude of 59.4 dB on curve 1. The third peak shows a maximum amplitude of 60.5 dB on curve 3 and a minimum amplitude of 52.6 dB on curve 1. The fourth peak shows a maximum amplitude of 56.5 dB on curve 4 and a minimum amplitude of 48.2 dB on curve 1. In general, the tonal amplitudes for curves 2, 3, and 4 were relatively close whereas the tonal amplitude for curve 1 was consistently significantly lower than the rest. The broadband levels also appear to be different between the curves. Curves 1 and 2 show similar broadband levels between the first and second harmonics but are different from those of curves 3 and 4. The broadband levels between the second and third harmonic are similar for curves 1, 2, and 3 but lower than those of curve 4. The broadband levels between the third and fourth harmonic are similar for curves 2, 3, and 4 but greater than those of curve 1.

These data selected featured a fixed fan speed and steady advance ratio and alignment angle. It was expected these curves would show consistent features based on the similar values of the independent variables. The observations from Fig. 17 suggest differences between all four curves on specific regions of the spectrum. One possible explanation could be changes in the turbulence properties of the ingested flow for fixed advance ratio and wind alignment values. Noise source mechanisms of open-rotor blades are influenced by turbulence properties. For instance, the far-field spectrum produced by an airfoil in a turbulent stream is affected by the integral length scale of the turbulence. Glegg and Devenport [14] explain that a change in the integral length scale of the turbulence causes a change in the overall level but also the shape of the spectrum. They show how an increase in the turbulence length scale can increase the low-frequency levels while reducing the high-frequency content of the spectrum. The influence of changes in integral length scales of turbulence on the noise generated by the OR-ANCF rotor blades could explain why for fixed independent variables, the SPL spectrum shows different levels in Fig. 17. Future measurements will include turbulence quantities to provide a wider view of the independent variables influencing noise generation by the OR-ANCF test article and help explain phenomena such as shown in Fig. 17.

Figure 18 shows the Overall Sound Pressure Level (OASPL) measured with the phased array. The data also correspond to a fan speed of 800 RPM, an advance ratio of $J = 0.19$, and alignment of $\theta_{align.} = -5°$. The image is colored based on the OASPL amplitude. The gray is associated with the minimum OASPL of 25 dB. The white is associated with the maximum OASPL of 35 dB. The image shows the OR-ANCF at the test site. The OR-ANCF is shown in alignment with the incoming wind direction. The alignment is evidenced by the alignment of the wind turbines shown in the background. There are white regions shown in the image. The regions are shown on the ground, on the back of the ANCF shaft, and at the test article. The test article is not visible due to the presence of the Kevlar screen between the camera and the test article. The radiated noise is measured by the phased array despite the presence of the Kevlar screen. The Kevlar screen has an unknown acoustic attenuation factor but it appears to have decent acoustic transparency.

There is a white region observed on the ground. This region is associated with ground reflections of the noise radiated by the test article. This reflection is the motivation for ground microphones. There is also a white region observed towards the aft end of the ANCF shaft. This is associated with gearbox noise and represents an additional noise source to the test article. Every other region around the noise and reflection regions is colored

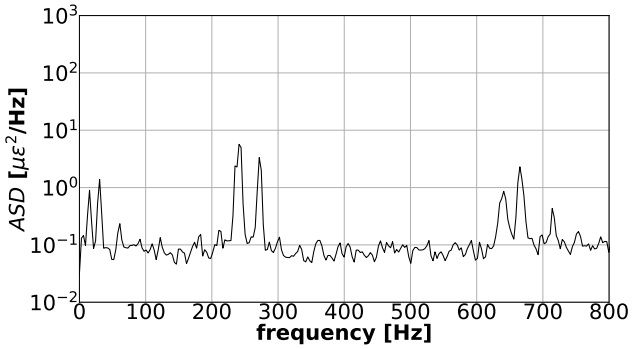

FIGURE 19: AUTO-SPECTRAL DENSITY OF STRAIN GAUGE 8 DATA FOR A FAN SPEED OF 1800 *RPM*, AN ADVANCE RATIO J = 0.32, AND WIND ALIGNMENT $\theta_{align.}$ = ±5°.

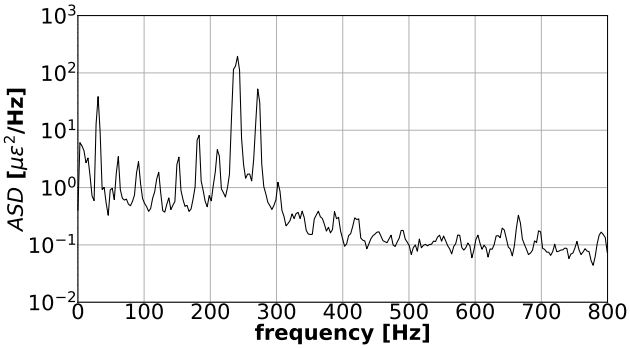

FIGURE 20: AUTO-SPECTRAL DENSITY OF STRAIN GAUGE 1 DATA FOR A FAN SPEED OF 1800 *RPM*, AN ADVANCE RATIO J = 0.32, AND WIND ALIGNMENT $\theta_{align.}$ = ±5°.

in gray. This color suggests that there are no relevant acoustic reflections from the structures in the vicinity of the ANCF facility. This observation suggest operating the OR-ANCF in an outdoor environment in the vicinity of multiple structures does not significantly influence the radiated noise measurements.

6.3 Aeromechanical response

Figure 19 shows the Auto-Spectral Density for the signal of strain gauge 8. Strain gauge 8 corresponds to the rotor blade 5 and location 2 on the blade. The Auto-Spectral was estimated for a period of 5 $secs$. The data correspond to a fan speed of 1800 RPM, an average advance ratio of $J = 0.16$, and an average alignment of $\theta_{align.} = -10°$ during the 5 sec. period. The abscissa shows the frequency in Hz. The abscissa is shown in dimensional form to allow comparison to the values of the multiple blade vibrational mode frequencies. The ordinate shows the Auto-Spectral Density amplitude in $\frac{(\mu\epsilon^2)}{Hz}$. The plot shows four prominent peaks. The peaks rise from the background by at least half an order of magnitude. The peaks are observed at frequencies of 30 Hz, 240 Hz, 640 Hz, and 668 Hz. The amplitude of the peaks are $1.3x10^0$ $\frac{\mu\epsilon^2}{Hz}$, $4x10^0$ $\frac{\mu\epsilon^2}{Hz}$, $1.8x10^0$ $\frac{\mu\epsilon^2}{Hz}$, and $1.8x10^0$ $\frac{\mu\epsilon^2}{Hz}$, respectively. There are lower peaks associated with integer values of the 30 Hz peak. The peak shown at a frequency 30 Hz coincides with the fan shaft rotation rate. The peaks observed at frequencies of 240 Hz, 640 Hz, and 668 Hz coincide with the natural frequencies of the blade of 235 Hz, 643, and 667 Hz predicted by the FEM modal analysis. The amplitude of the peak associated with the fan rotation rate appears to dominate the amplitudes of the blade vibrational modes. The amplitudes of the blade vibrational frequencies are proportional to the visibility matrix for the strain gauge location.

Figure 20 shows the Auto-Spectral Density for the signal of strain gauge 1 in the same format a Fig. 19. The plot shows two prominent peaks. The peaks rise from the background by at least half an order of magnitude. The peaks are observed at frequencies of 30 Hz and 240 Hz. The amplitude of the peaks are $4x10^1$ $\frac{\mu\epsilon^2}{Hz}$ and $1.25x10^2$ $\frac{\mu\epsilon^2}{Hz}$, respectively. The peak at 30 Hz coincides with the fan rotation rate. There are other peaks associated with integer values of the 30 Hz peak. There are smaller peaks at 640 Hz and 668 Hz observed as well but their amplitudes are significantly lower than the other peaks. Their amplitudes are $2.4x10^1$ $\frac{\mu\epsilon^2}{Hz}$ and $2.4x10^1$ $\frac{\mu\epsilon^2}{Hz}$, respectively. The peak at 240 Hz coincides with the frequency of the first vibrational mode of the rotor blade. These data show that the natural frequencies of the blade were excited during the OR-ANCF test article operation. The vibrations of the rotor blades were captured by the strain gauge and their amplitudes were consistent with the visibility matrix that guided their placement along the rotor blades.

7. CONCLUSION

The venerable Advanced Noise Control Fan was successfully re-purposed to operate an open-rotor configuration in an outdoor environment. An open-rotor blade set was designed and evaluated. Additional instrumentation was added to account for the ambient conditions.

The proof-of-concept and initial operating capability tests showed that uncontrollable wind conditions do not represent an impediment to outdoor open-rotor testing. The strategies employed for wind measurements and analyses can be followed by other open-rotor testing facilities to address similar challenges. For instance, historical wind data plays a key role in understanding the expected conditions at a given test site and designing for an advance ratio. For the work presented in this paper, the historical data informed the selection of the design advance ratio as a trade-off between desired flow field characteristics and relevant noise levels. The results also highlighted the relevance of a low TRL facility for open-rotor research. The multi-fidelity design loop represents a tool to output a variety of open-rotor test article geometries at relatively low costs. In the case of the work presented in this paper, the design loop was used to provide a test article that complied with aeromechanical, aerodynamic, and aeroacoustic criteria. The measurement capabilities of the ANCF facility successfully captured the acoustic signature and vibrational response of the open-rotor test article as a function of the unsteady and uncontrollable wind conditions.

Future work utilizing the OR-ANCF test article and the collected data will cover a wide range of areas. One focus will be the development and implementation of a Neural Network to provide regression between the measured data. This Neural Network is

expected to fill in the gaps in the sparse data obtained from outdoor tests. Another area will involve further analysis of the existing data, particularly studying the impact of rotor blade pitch angle changes on the aeroacoustic and aeromechanical responses. This aspect remains to be explored by processing the existing data. Additional efforts will also include acquiring data for additional physical parameters, supported by expanded measurement capabilities that will capture thrust and torque, blade surface pressure, and incoming wind turbulence properties. Another important focus will be outdoor tests involving a single-stage open-rotor test article, which will incorporate both rotor blades and additively manufactured stator vanes. Finally, future work will include generating Computational Aeroacoustic (CAA) predictions for the OR-ANCF test article and comparing these predictions to the measured radiated noise.

ACKNOWLEDGMENTS

This effort was supported by the NASA Aeronautics Research Mission Directorate Advanced Air Vehicle Program/Advanced Aircraft Transport Technology Project/ Propulsion Technologies sub-Project/ EQuIP Technical Challenge. The staff of NDTL Propulsion and Power are acknowledged for supporting the design, build, and operation of the open-rotor ANCF facility. The authors would like to acknowledge the consultations provided by Dr. Trevor Wood, GE Aerospace Research, Dr. Takao Suzuki, The Boeing Company, and Dr Mark Turner, NASA Glenn Research Center, that helped ensure the relevancy of the Un-Ducted/Open Rotor Advanced Noise Control Fan test article. The authors would also like to thank the Career Academy Network of Public Schools (CANoPS) for providing additively manufactured stator vanes that will be utilized in the open-rotor test article.

Research was sponsored by the National Aeronautics and Space Administration (NASA) through a contract with ORAU. The views and conclusions contained in this document are those of the authors and should not be interpreted as representing the official policies, either expressed or implied, of the National Aeronautics and Space Administration (NASA) or the U.S. Government. The U.S. Government is authorized to reproduce and distribute reprints for Government purposes notwithstanding any copyright notation herein.

REFERENCES

[1] Brown, Cliff, Reinert, Jess, Stephens, David and Dumlupinar, Ercan. "NASA's Efficient Quiet Integrated Propulsors (Equip) Technical Challenge." *34th Congress of the International Council of the Aeronautical Sciences (ICAS)*. 2024.

[2] Sutliff, Daniel L. "Advanced noise control fan: a 20-year retrospective of contributions to aeroacoustics research." Technical report no. NASA. 2019.

[3] Sutliff, Daniel L. "A 20 year retrospective of the advanced noise control fan–contributions to turbofan noise research." *AIAA Propulsion and Energy 2019 Forum*: p. 3824. 2019.

[4] Figueroa-Ibrahim, Kelvin M, Morris, Scott, Ross, Mark and Sutliff, Daniel L. "Evaluation of radiated sound from the advanced noise control fan facility in an outdoor environment using ground microphones." *AIAA Propulsion and Energy 2019 Forum*: p. 3825. 2019.

[5] Sutliff, Daniel L, Brown, Clifford A, Figueroa-Ibrahim, Kelvin, Morris, Scott, Ross, Mark and Wang, Ryne. "Conversion of the Advanced Noise Control Fan to an Open Rotor Configuration in Support of NASA's Efficient Quiet Integrated Propulsor Technical Challenge." *30th AIAA/CEAS Aeroacoustics Conference (2024)*: p. 3099. 2024.

[6] Xuan, Haijun, Hu, Yanqi, Wu, Yanan and He, Zekan. "Containment ability of Kevlar 49 composite case under spinning impact." *Journal of Aerospace Engineering* Vol. 31 No. 2 (2018): p. 04017096.

[7] Wicklund, Victor. *Unwanted In-Flight Thrust Reversal of Turbojet Thrust Reversers*. U.S. Department of Transportation (2012). URL https://www.faa.gov/sites/faa.gov/files/2022-12/DRAFT_AC25.933-X.pdf.

[8] Seng, Silvia, Frankenberger, Charles, Ruggeri, Charles R, Revilock, Duane M, Pereira, J Michael, Carney, Kelly S and Emmerling, William C. "Dynamic Open-Rotor Composite Shield Impact Test Report." Technical report no. 2015.

[9] Stotler, C. "Development of advanced lightweight containment systems." Technical report no. 1981.

[10] Smith, GT. "Composite containment systems for jet engine fan blades." *Ann. Conf. of the Reinforced Plastics/Composites Inst. of the Soc. of the Plastics Ind., Inc.,*. E-700. 1981.

[11] Zekan, HE, Haijun, XUAN, Conger, BAI, Manli, SONG and Zhuoshen, ZHU. "Containment of soft wall casing wrapped with Kevlar fabric." *Chinese Journal of Aeronautics* Vol. 32 No. 4 (2019): pp. 954–966.

[12] Seguro, JV and Lambert, TW. "Modern estimation of the parameters of the Weibull wind speed distribution for wind energy analysis." *Journal of wind engineering and industrial aerodynamics* Vol. 85 No. 1 (2000): pp. 75–84.

[13] Siddappaji, Kiran and Turner, Mark. "Multifidelity Analysis of a Solo Propeller: Entropy Rise Using Vorticity Dynamics and Kinetic Energy Dissipation." *Fluids* Vol. 7 No. 5 (2022): p. 177.

[14] Glegg, Stewart and Devenport, William. *Aeroacoustics of low Mach number flows: fundamentals, analysis, and measurement*. Academic Press (2017).

[15] Blake, William K. *Mechanics of flow-induced sound and vibration, Volume 2: Complex flow-structure interactions*. Academic press (2017).

[16] Brooks, Thomas F and Marcolini, Michael A. "Airfoil tip vortex formation noise." *AIAA journal* Vol. 24 No. 2 (1986): pp. 246–252.